

Exploring dust formation in the episodic WCd system WR140

J. W. Eatson[★] & J. M. Pittard

School of Physics and Astronomy, University of Leeds, Woodhouse Lane, Leeds LS2 9JT, UK

Accepted XXX. Received YYY; in original form ZZZ

ABSTRACT

Key words: stars: Wolf-Rayet – methods: numerical – binaries: general

1 INTRODUCTION

The dynamics of massive stars in binary systems is a particularly fascinating subject. These incredibly violent systems are obscured behind vast clouds of outflowing stellar wind, the result of the most massive stars we know of slowly tearing themselves asunder. Despite powerful winds, extreme temperatures, and intense astrophysical shocks from these colliding winds, interstellar dust

In fact, these dust producing CWB (WCd) systems can produce an extreme quantity of dust. Typically around 1% of the stellar wind is converted into dust a short amount of time after wind collision, but in the case of more prolific systems such as WR104 this can be as high as 36% (Lau et al. 2020). This corresponds to dust production rates on the order of $10^{-6} M_{\odot} \text{ yr}^{-1}$, rivalling other profuse dust producing phenomena such as AGB stars.

While we know that truly colossal amounts of dust form in these systems through infrared observation, we find that the mechanisms involved in

Observations conclude that dust forms exclusively within the WCR of the system, observations also indicate that dust formation occurs rapidly and close to the system (Williams et al. 1987, 1990),

this is further backed up by grain

In this paper we will discuss our methodology in section

2 METHODOLOGY

The periodic dust forming system WR140 was simulated using a fork of the Athena++ hydrodynamical code (Stone et al. 2020), a series of modifications were implemented to simulate binary system orbits, stellar wind outflows and dust evolution. These simulations were conducted in 3D in a Cartesian co-ordinate system. The code solves a Riemann problem at each cell interface to determine the time-averaged values at the zone interfaces, and then solves the equations of hydrodynamics:

$$\frac{\partial \rho}{\partial t} + \nabla \cdot (\rho \mathbf{u}) = 0, \quad (1a)$$

$$\frac{\partial \rho \mathbf{u}}{\partial t} + \nabla \cdot (\rho \mathbf{u} \mathbf{u} + P) = 0, \quad (1b)$$

$$\frac{\partial \rho \varepsilon}{\partial t} + \nabla \cdot [\mathbf{u} (\rho \varepsilon + P)] = \dot{E}_{\text{cool}}, \quad (1c)$$

where ε is the total specific energy ($\varepsilon = \mathbf{u}^2/2 + e/\rho$), ρ is the gas density, e is the internal energy density, P is the gas pressure and \mathbf{u} is the gas velocity. In order to simulate radiative losses, the parameter \dot{E}_{cool} is included, which is the energy loss rate per unit volume from the fluid due to gas and dust cooling.

Spatial reconstruction using a piecewise linear method was performed, while the time-integration scheme is a third-order accurate, three-stage strong stability preserving Runge-Kutta¹ method (Gottlieb et al. 2009). Several passive scalars are utilised to model wind mixing and dust evolution, the scalar values are transported by the fluid, for a given scalar species i , the scalar is advected through the scalar through the following equation:

$$\rho \frac{dC_i}{dt} = \frac{\partial}{\partial t} (\rho C_i) + \nabla \cdot (C_i \rho \mathbf{u}) = -\nabla \cdot \mathbf{Q}_i, \quad (2)$$

where $\mathbf{Q}_i = -\nu_{ps} \rho \nabla C_i$ is the diffusive flux density and ν is the passive scalar diffusion coefficient (Stone et al. 2020).

Stellar winds are simulated by modifying the density, ρ_R , momentum, p_R , and energy, E_R in a small region around both stars. Winds flow from this “remap” region at the stars wind terminal velocity, v^{∞} . Remap zone parameters are calculated with the formulae

$$\rho_R = \frac{\dot{M}}{4\pi r^2 v_{\infty}}, \quad (3a)$$

$$p_R = \rho_R v_r, \quad (3b)$$

$$E_R = \frac{P_R}{\gamma - 1} + \frac{1}{2} \rho_R v_{\infty}^2, \quad (3c)$$

where P_R is the cell pressure, $P_R = \rho_R k_B T_w / \mu m_H$, T_w is the wind temperature, μ is the mean molecular mass, m_H is the mass of a hydrogen atom, v_R is the wind velocity as it flows radially

[★] E-mail: py13je@leeds.ac.uk

¹ SSPRK (3,3)

from the center of the “remap zone” and r is the distance from the current cell to the centre of the remap zone. This method produces radially out-flowing winds from the star with an expected density and velocity. This method is stable against numerical instability, while also allowing us to precisely control the winds.

Line driving and wind acceleration effects are not simulated, which can result in divergence with the correct wind velocity as stars approach periastron passage. Instead, winds are instantaneously accelerated to their terminal velocity. Additionally, influence from either gravitational self-interaction and interaction with the stars gravity wells is not simulated, with the stellar winds assumed to be travelling far in excess of the system escape velocity.

Athena++ utilises Message Passing Interface (MPI) parallelism. The numerical problem is broken into blocks, which are distributed between processing nodes on a High Performance Compute (HPC) cluster. The block size is variable, but for these simulations a block size of $40 \times 40 \times 10$ cells in XYZ was found to be optimal. Adaptive Mesh Refinement was considered for this simulation, however a known issue with the Athena++ code prevented this from being possible. Passive scalars incorporated into the simulation were found to not be conserved along the interfaces between mesh blocks undergoing refinement, this meant that the simulation would behave non-physically (This bug is recorded as issue #365 on the Athena++ Github repository²). A ring of refined cells across the orbital path was considered, but the performance improvements of this method were found to be negligible and not worth pursuing, as the block based refinement method of Athena++ would result in much redundant refinement. Instead, a static mesh is used, where the stars predicted orbit over the simulation is refined to the maximum level, with a gradual de-refinement away from this refinement region.

2.1 Radiative cooling

Cooling is simulated via the removal of energy from a cell at each time-step. A cooling rate, dE/dt , is calculated, and integrated using a sub-stepping Euler method, with the number of sub-steps determined by the estimated cooling timescale of the cell. Cooling due to gas and plasma emission in the stellar winds are calculated via individual lookup tables from each wind. These lookup tables contain the normalised emissivity, $\Lambda_w(T)$ for a specific temperature from 10^4 to 10^9 K. The cooling rate is determined for a cell by calculating the cell temperature, and estimating $\Lambda_w(T)$ using linear interpolation between the nearest emissivity values in the lookup table. The energy loss is then calculated through the equation

$$\frac{dE}{dt} = \left(\frac{\rho}{m_H} \right)^2 \Lambda_w(T), \quad (4)$$

where ρ is the gas density and m_H is the mass of hydrogen. The lookup table was generated by mixing a series of cooling curves from MEKAL simulations of elemental gasses. These curves were combined based on the elemental abundances in the WC and OB winds. To save calculation time, temperatures between 1×10^4 K < $T \leq 1.1 \times 10^4$ K are set to 1×10^4 K as they are assumed to be either rapidly cooling or a part of the stellar wind outside of the WCR.

2.2 Dust model

In order to simulate dust evolution in WR140, included in the hydrodynamical code is a passive scalar dust model that simulates dust growth through collisions between dust grains and carbon atoms, and destruction through sputtering from a hot wind. The dust model operates on passive scalars, and as such simulates dust that is co-moving with the stellar wind. Two scalars are used to describe dust in a cell, a , the grain radius in μm , and z , the grain dust-to-gas mass ratio:

$$z = \frac{\rho_d}{\rho_g}, \quad (5)$$

where ρ_d is the dust density in a cell and ρ_g is the gas density in a cell. A number of assumptions are made in this dust model, for instance, the dust grains in the model are spherical, with a uniform density. Furthermore, dust grains are assumed to have a single size in a region, as well as a constant number density. As such, this model does not simulate grain agglomeration and fracturing. Additional mechanisms for dust formation and destruction could also be implemented such as grain-grain agglomeration and photoevaporation. A multi-fluid model with drag force coupling could also be implemented, however this is beyond the scope of this paper.

Dust is grown through grain accretion using formulae described by (Spitzer 2008) where dust grains grow via low-velocity collisions with surrounding carbon atoms, causing them to accrete onto the surface of the dust grain. Carbon is removed from the gas, reducing the cell density, while the corresponding dust density increases. This ensures that mass is preserved in the simulation. Assuming a single average grain size the rate of change in the grain radius in a cell, da/dt , is given by the equation:

$$\frac{da}{dt} = \frac{\xi \rho_C w_C}{4 \rho_{gr}}, \quad (6)$$

where ξ is the grain sticking factor, ρ_C is the carbon density ($\rho_C = X_C \rho_g$), w_C is the Maxwell-Boltzmann RMS velocity for carbon ($w_C = \sqrt{3k_B T / 12m_H}$), k_B is the Boltzmann constant and ρ_{gr} is the grain bulk density. The rate of change in grain mass due to accretion, $dm_{gr,ac}/dt$, is calculated with the formulae:

$$\frac{dm_{gr,ac}}{dt} = 4\pi \rho_{gr} a^2 \frac{da}{dt} = \pi \xi \rho_C w_C a^2, \quad (7)$$

A bulk density approximating that of amorphous carbon grains ($\rho_{gr} = 3.0 \text{ g cm}^{-3}$) is used for this simulation.

Dust destruction gas-grain sputtering is calculated using the Draine & Salpeter (1979) prescription. Within a flow of number density n_g a dust grain of radius a has a grain lifespan, τ_{gr} of:

$$\tau_{gr} = \frac{a}{\dot{a}} \approx 3 \times 10^6 \frac{a}{n_g} \text{ yr}. \quad (8)$$

This value is based on an average lifetime of carbon grains in an interstellar shock with a temperature of $1 \times 10^6 \text{ K} \leq T \leq 3 \times 10^8 \text{ K}$ (Tielens et al. 1994; Dwek et al. 1996). The rate of change in the dust grain mass due to sputtering, $dm_{gr,sp}/dt$, can then be calculated with a similar formulae to the rate of change in grain mass due to accretion:

$$\frac{dm_{gr,sp}}{dt} = 4\pi \rho_{gr} a^2 \frac{da}{dt} = -4\pi \tau_{gr} n_g a^2. \quad (9)$$

Finally, the total rate of change in grain mass is calculated, the overall change in dust density is then calculated:

² <https://github.com/PrincetonUniversity/athena/issues/365>

$$\frac{d\rho_d}{dt} = \left(\frac{dm_{\text{gr,acc}}}{dt} + \frac{dm_{\text{gr,sp}}}{dt} \right) n_d, \quad (10)$$

where n_d is the dust grain number density.

Cooling via emission of photons from dust grains is also included in this model. The rate of cooling is calculated using the uncharged grain case of the prescription described in (Dwek & Werner 1981). Grains are collisionally excited by collisions with ions and electrons, causing them to radiate. Similarly to the gas/plasma emission model used, the emitted photons are not re-adsorbed by the WCR medium, causing energy to be removed from the simulation. This therefore makes the assumption that the WCR is optically thin to far-infrared photons, which is observationally correct. The grain heating rate (in erg s^{-1}) for a dust grain is calculated with the formulae:

$$H = 1.26 \times 10^{-19} \frac{n_g}{A^{1/2}} a^2 (\mu\text{m}) T^{3/2} h(a, T), \quad (11)$$

where H is the heating rate due to atom and ion collisions, n is the particle number density, A is the mass of the incident particle in AMU, $a(\mu\text{m})$ is the grain radius in microns, T is the temperature of the ambient gas, and $h(a, T)$ is the effective grain heating factor. Individual heating rates for hydrogen, helium, carbon, nitrogen and oxygen are calculated, in order to calculate the total ion collisional heating, H_{coll} :

$$H_{\text{coll}} = H_{\text{H}} + H_{\text{He}} + H_{\text{C}} + H_{\text{N}} + H_{\text{O}}. \quad (12)$$

The effective grain heating factor for each element is calculated via the equation:

$$h(a, T) = 1 - \left(1 + \frac{E^*}{2k_{\text{B}}T} \right) e^{-E^*/k_{\text{B}}T}, \quad (13)$$

where E^* is the critical energy required to overcome the grain's potential (Table 1). The rate of heating due to electron-grain collisions, H_{el} , is similar to Eq. 11. The grain heating factor for electron collisions, h_e , is calculated via an approximation from Dwek & Werner (1981). This approximation is performed as a complex integration for every cell and cooling step would need to be performed instead, which was found to take up > 90% of the processing time for a cell. h_e is estimated through the following conditions:

$$\begin{aligned} h_e(x^*) &= 1, & x^* &> 4.5, \\ &= 0.37x^{*0.62}, & x^* &> 1.5, \\ &= 0.27x^{*1.50}, & \text{otherwise,} \end{aligned} \quad (14)$$

where $x^* = 2.71 \times 10^8 a^{2/3} (\mu\text{m}) / T$. This approximation differs from the integration method by less than 8% while being 4 orders of magnitude faster. Excitation due to grain-grain collisions were not modelled, due to the limitations of the passive scalar model. In order to calculate the change in energy due to dust cooling, we find the radiative emissivity for dust, $\Lambda_d(T, a)$, to be:

$$\Lambda(T, a) = \frac{H_{\text{coll}} + H_{\text{el}}}{n_{\text{H}}} \quad (15)$$

where n_{H} is the number density of hydrogen in the gas. The energy loss rate from dust cooling, dE_d/dt , then calculated with the equation:

Particle	E^*
e^-	$23 a^{2/3} (\mu\text{m})$
H	$133 a (\mu\text{m})$
He	$222 a (\mu\text{m})$
C	$665 a (\mu\text{m})$
N	$665 a (\mu\text{m})$
O	$665 a (\mu\text{m})$

Table 1. Grain potential critical energy, E^* , for a dust grain of a in μm for electrons, e^- , as well as the elements considered for grain cooling. The values for carbon, oxygen and nitrogen are identical.

Parameter	Value	Citation
M_{WR}	$10.31 M_{\odot}$	Thomas et al. (2021)
M_{OB}	$29.27 M_{\odot}$	Thomas et al. (2021)
P	7.926 yr	Thomas et al. (2021)
e	0.8993	Thomas et al. (2021)
\dot{M}_{WR}	$5.6 \times 10^{-5} M_{\odot} \text{ yr}^{-1}$	Williams et al. (1990)
\dot{M}_{WR}	$1.6 \times 10^{-6} M_{\odot} \text{ yr}^{-1}$	Williams et al. (1990)
v_{WR}^{∞}	$2.86 \times 10^3 \text{ km s}^{-1}$	Williams et al. (1990)
v_{OB}^{∞}	$3.20 \times 10^3 \text{ km s}^{-1}$	Williams et al. (1990)
η	0.031	Calculated
χ_{min}	2.69	Calculated

Table 2. WR140 system parameters.

$$\frac{dE_d}{dt} = n_{\text{T}} n_d \Lambda_d(T, a), \quad (16)$$

and summated with the gas/plasma energy loss rate.

3 WR140 AND SIMULATION PARAMETERS

WR 140 was simulated in this paper as it is considered to be the archetypical episodic CWB system, whose infrared dust emission peaks around periastron passage. WR 140 deviates from WR 98a and WR 104 by having an extremely eccentric orbit, which significantly effects the cooling parameter as the orbit progresses. Additionally, the minimum value for χ is significantly larger than the other systems, and hence cooling would be less dominant on the dynamics of the WCR, even at periastron.

Though these simulations do not calculate wind acceleration due to radiative line driving, both stellar winds are expected to be accelerated close to their terminal wind velocities (Lamers & Cassinelli 1999). However, this discrepancy should be noted when considering the results of this paper.

3.1 System parameters

Recent improved estimations of the orbital parameters of WR140 by Thomas et al. (2021) were used to calculate the orbital path for these simulations, while the mass loss rate, \dot{M} , and the wind terminal velocity, v^{∞} , were derived from Williams et al. (1990) (Table 2). In order to correctly calculate cooling and dust growth, the abundances of hydrogen, helium, and metals, particularly CNO must be included in the simulations parameters. A typical wind composition for WC stars was assumed for the Wolf-Rayet star, while a solar abundance was assumed for the OB star (Table 3). The system orbit was calculated using a Keplerian orbital model with the two stars as point-masses.

Element	Solar	WC
X_H	0.705	0.000
X_{He}	0.275	0.546
X_C	0.003	0.400
X_N	0.001	0.000
X_O	0.010	0.050

Table 3. Abundances used for the OB and WR stars being simulated. Other elements are assumed trace when calculating dust emission (Williams et al. 2015).

3.2 Simulation parameters

A domain of $128 \times 128 \times 16$ AU was used for this simulation, with a coarse simulation resolution of $400 \times 400 \times 50$ in the XYZ domain. This simulation has an XY to Z aspect ratio of 8:1 in order to reduce processing time, as the bulk of dust formation was expected to occur a short distance from the WCR. Due to computing limitations, a complete orbit could not be completed without AMR, instead, a section of the systems orbit, corresponding to an orbital phase of $0.95 \leq \Phi \leq 1.10$ was simulated, where Φ is the orbital phase. This section represents the period prior to periastron passage, as well as a brief period after periastron (Fig. 1). This represents a period of approximately 1.2 years of the systems orbit, and the period where much of the dust forms (Crowther 2003). Fig. 2 shows the orbital path overlaid onto the statically refined numerical grid, the area of maximum refinement is around the orbital paths of the stars from $0.94 \leq \Phi \leq 1.11$, in order to ensure that the stars are maximally refined. If the stars leave the maximally refined region of the simulation unphysical behaviour with regards to wind mapping and dust formation occur, as such the simulation is halted when $\Phi = 1.10$. The simulation was run with two different numerical integrators, a 3rd order accurate Runge-Kutta integrator (rk3) and a 4th order accurate, 5-stage, 3 storage register strong stability preserving Runge-Kutta integrator (ssprk5_4) (Ruuth & Spiteri 2005). The ssprk5_4 integrator was found to be approximately 60% slower, but markedly more stable. Prior to periastron passage the rk3 integrator was used for its speed, but increasing numerical instability as the stars grew closer resulted in this proving untenable, and was switched to ssprk5_4.

Over periastron passage the average time-step was found to reduce by an order of magnitude, resulting in a corresponding increase to simulation time (Fig. 3). At the most numerically complex portion of the simulation, a Courant number of $C = 0.04$ had to be used instead of the initial value of $C = 0.15$, in order to preserve numerical stability. As the simulation moved past periastron the Courant number was increased every 24 hours of wall time, until C returned to the initial value. The simulation was conducted on the ARC4 HPC cluster at the University of Leeds with 128 cores. The code was compiled using the Intel ICPC compiler using AVX512 optimisations and the Intel MPI library.

3.3 Data collection

Simulation data was exported in the form of HDF5 at regular time intervals - 3D HDF5 meshes were collected every increment of $\Phi = 1.5 \times 10^{-3}$, while 2D slices in the XY plane were collected every increment of $\Phi = 1.5 \times 10^{-4}$. These HDF5 files contain the primitive variables of the simulation: gas density, ρ , gas pressure, P , and wind velocity components, v_x , v_y and v_z . These variables were then used to derive other variables such as temperature and energy. The scalars governing the dust properties were also stored for each cell: the dust-to-gas mass ratio, z , and the dust grain radius, a . The wind “colour”, the proportion of gas from each star, was also tracked. A value of

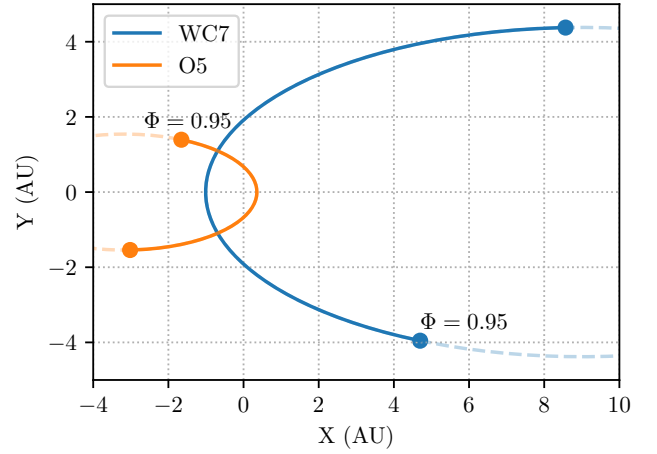


Figure 1. Simulation orbital trajectories of the WC7 and O5 stars in WR140. The solid line represents the orbital phase being simulated, corresponding to $0.95 \leq \Phi \leq 1.10$. The simulation starting position for each star has been annotated.

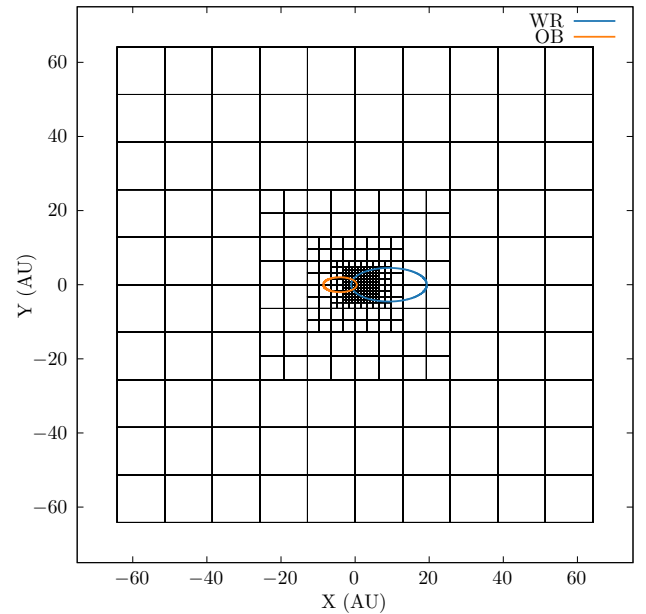


Figure 2. Numerical grid of the WR140 system simulation, static mesh refinement was used to increase the resolution around the orbital path from $0.95 \leq \Phi \leq 1.10$. The orbital path of both stars are overlaid onto this numerical grid. Beyond $\Phi = 1.11$ the WR star exits the fully refined region of the simulation, causing the simulation to break down.

1.0 indicates a pure WR wind while 0.0 indicates a pure OB wind. The volume-weighted totals of all parameters of interest were also collected, such as the average values for z , a and the dust production rate within the WCR, \dot{M}_d . To calculate \dot{M}_d , a cell must be identified as being within the WCR, this was performed by comparing the cell density to the predicted density of a single wind with the wind parameters of the WC star in the system. Any cell with a density higher a certain threshold value was flagged as being within the WCR. the single-wind density was calculated using the equation:

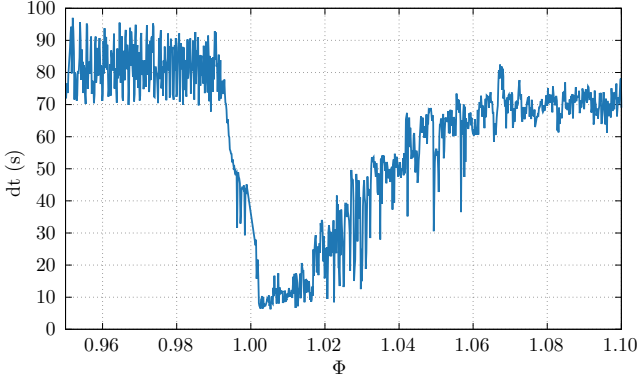


Figure 3. Average timestep, dt , over the course of the WR140 simulation, binned every $\Phi = 0.001$. After periastron passage the `ssprk5_4` numerical integrator and a drastically reduced Courant number was adopted in order to preserve numerical stability. This increased simulation time by approximately an order of magnitude.

Parameter	Mean	Maximum	Minimum
\dot{M}_d ($M_\odot \text{ yr}^{-1}$)	7.68×10^{-8}	1.24×10^{-6}	1.30×10^{-19}
\bar{a} (μm)	1.32×10^{-2}	1.44×10^{-2}	5.45×10^{-3}
\bar{z}	3.97×10^{-4}	3.32×10^{-3}	1.60×10^{-7}

Table 4. Advected scalar yields from the WR140 simulation.

$$\rho_{\text{SW}} = \frac{\dot{M}_{\text{SW}}}{4\pi r^2 v_{\text{SW}}^\infty}, \quad (17)$$

where r is the distance from the barycentre. This threshold value was set to $\rho_{\text{thres}} = 1.25\rho_{\text{SW}}$, which was found to accurately identify the WCR through prior testing.

4 RESULTS

4.1 Dust yields

The dust production were found to be consistent with the predictions made in our previous paper. After an initial advection period lasting until $\Phi \approx 0.96$, the dust production rate rapidly increased as the stars approached periastron passage, peaking at $\phi = 1.005$. After this maximum value, the

(Fig. 4)

This is reflected in the overall dust mass of the simulation (Fig. 5), as well as in infrared observations of WR140, where the infrared emission from dust formation rapidly reaches a maximum value after periastron passage, and slowly relaxes to a minimum value. This asymmetry in the time-dependent change in infrared luminosity implies the existence of several factors for suppression and encouragement of dust formation than the change in orbital separation distance.

It should be noted that due to the small size of the simulation, the dust mass in the system will reduce quickly, as dust advects off of the numerical grid.

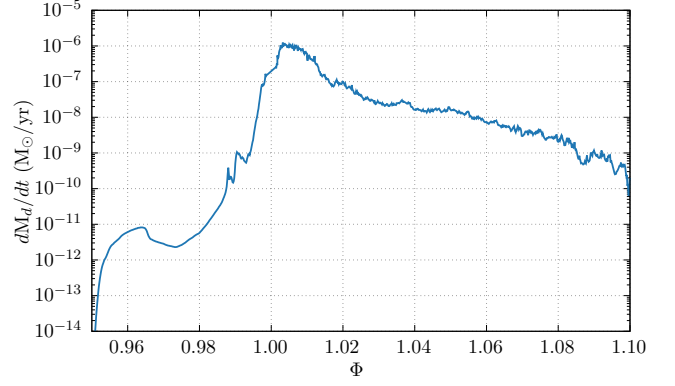


Figure 4.

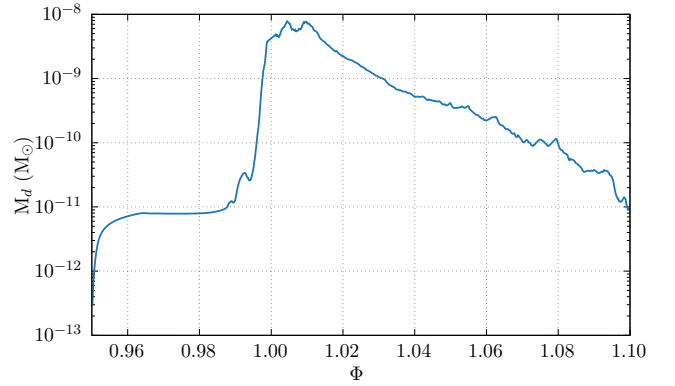
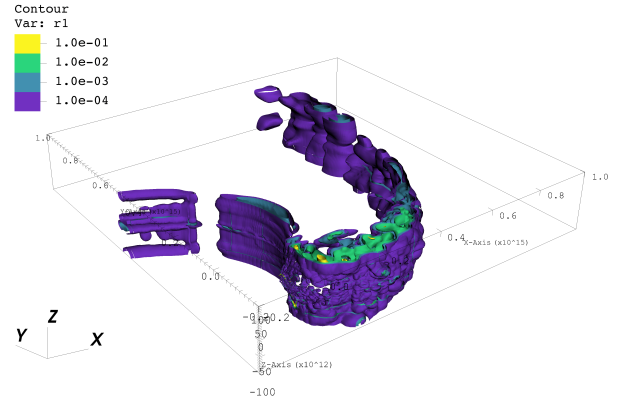


Figure 5.



4.2 Instabilities

4.3 Influence of radial velocity on dust production

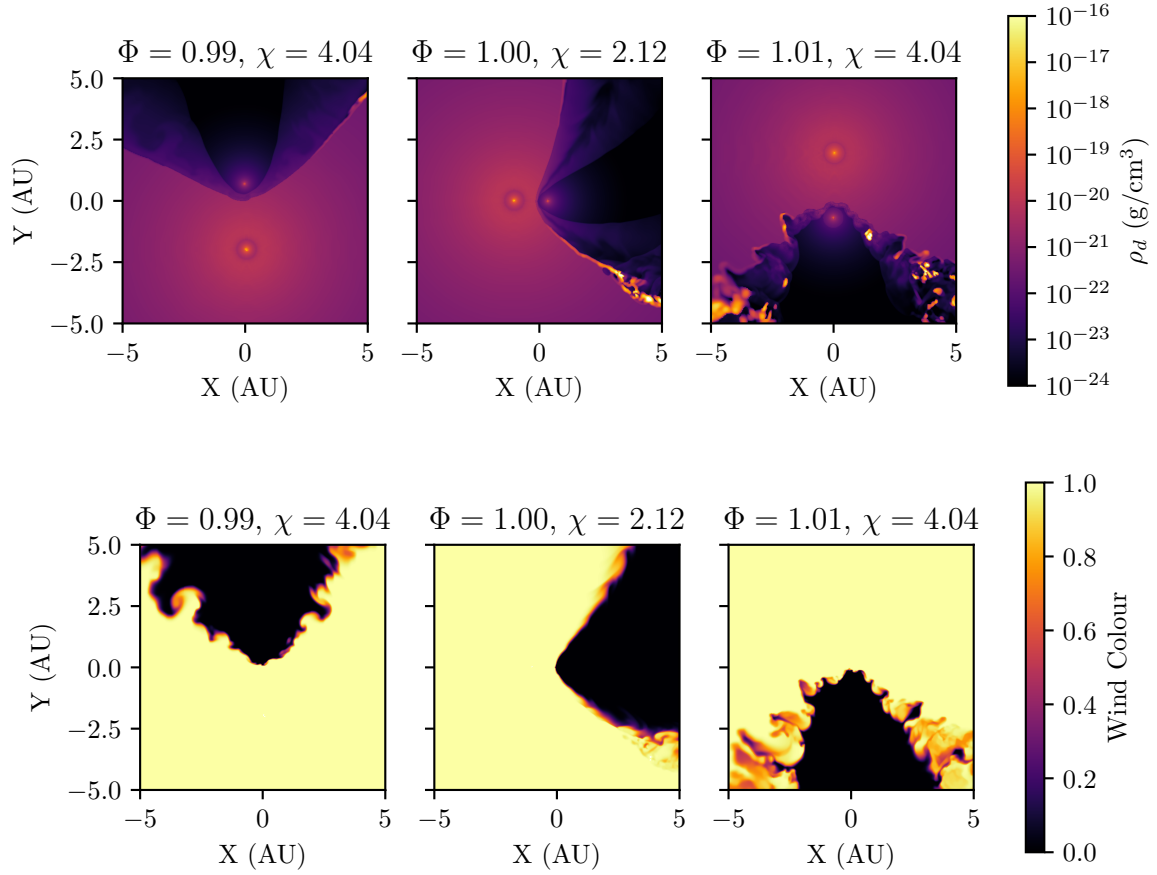
4.4 Other changes in velocity shear

5 CONCLUSION

6 ACKNOWLEDGEMENTS

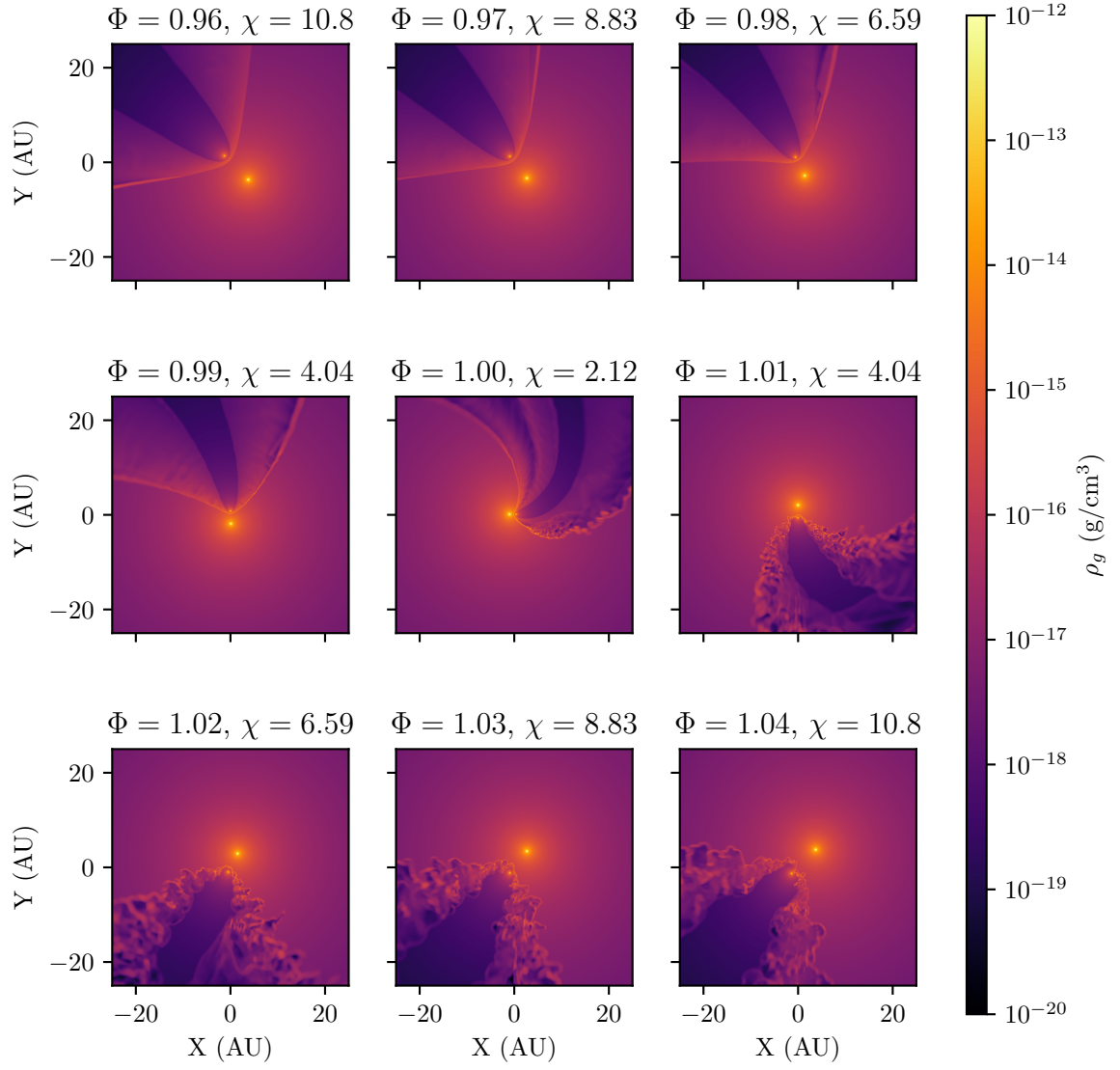
REFERENCES

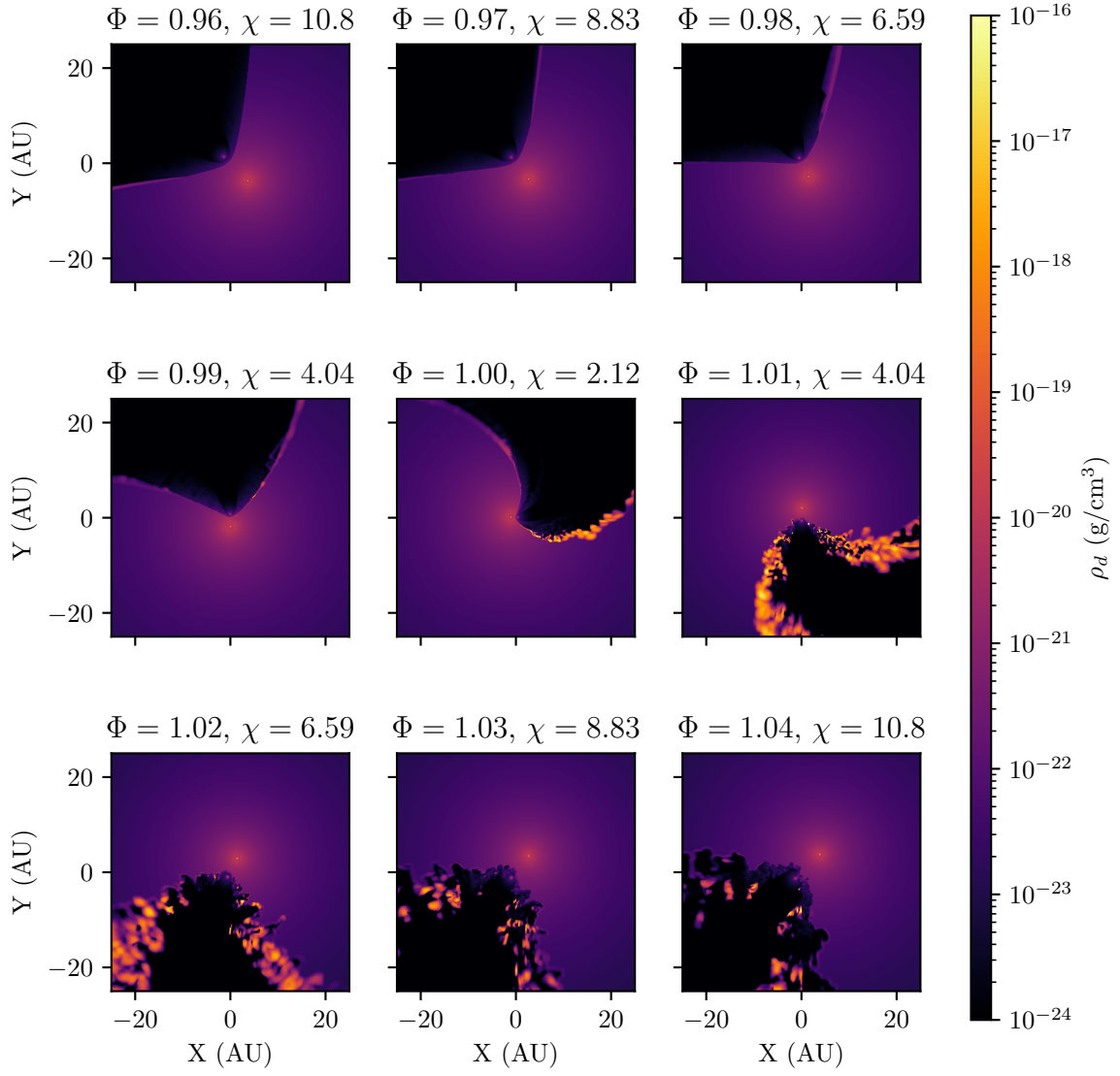
Crowther P. A., 2003, *Astrophysics and Space Science*, 285, 677



- Draine B. T., Salpeter E. E., 1979, *The Astrophysical Journal*, 231, 77
- Dwek E., Werner M. W., 1981, *The Astrophysical Journal*, 248, 138
- Dwek E., Foster S. M., Vancura O., 1996, *The Astrophysical Journal*, 457, 244
- Gottlieb S., Ketcheson D. I., Shu C.-W., 2009, *J Sci Comput*, 38, 251
- Lamers H. J., Cassinelli J. P., 1999, *Introduction to Stellar Winds*. Cambridge University Press
- Lau R. M., Eldridge J. J., Hankins M. J., Lamberts A., Sakon I., Williams P. M., 2020, *ApJ*, 898, 74
- Ruuth S. J., Spiteri R. J., 2005, *SIAM Journal on Numerical Analysis*, 42, 974
- Spitzer L., 2008, *Physical Processes in the Interstellar Medium*. John Wiley & Sons
- Stone J. M., Tomida K., White C. J., Felker K. G., 2020, *ApJS*, 249, 4
- Thomas J. D., et al., 2021, *Monthly Notices of the Royal Astronomical Society*, 504, 5221
- Tielens A. G. G. M., McKee C. F., Seab C. G., Hollenbach D. J., 1994, *The Astrophysical Journal*, 431, 321
- Williams P. M., van der Hucht K. A., Thé P. S., 1987, *Astronomy and Astrophysics*, 182, 91
- Williams P. M., van der Hucht K. A., Pollock A. M. T., 1990, *Monthly Notices of the Royal Astronomical Society*, 243, 662
- Williams P. M., Crowther P. A., van der Hucht K. A., 2015, *Monthly Notices of the Royal Astronomical Society*, 449, 1834

This paper has been typeset from a \LaTeX file prepared by the author.





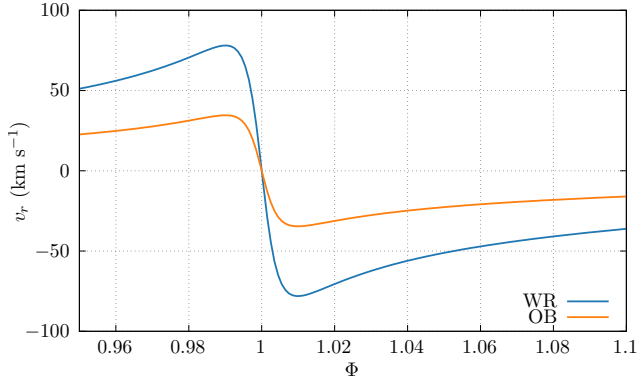


Figure 6. Radial velocity as a function of the orbital phase for the WR and OB stars in the WR140 system relative to the barycentre. As periastron passage occurs, the sudden inversion from approaching to receding can alter the wind velocity of the WR star by as much as 160 km s^{-1} . Whilst this discrepancy is $\sim 6\%$ of the WR wind velocity, this can significantly increase dust production if the stars are receding from each other.